ACS APPLIED MATERIALS & INTERFACES

Research Article

www.acsami.org

Multiphase and Double-Layer $NiFe_2O_4$@NiO-Hollow-Nanosphere-Decorated Reduced Graphene Oxide Composite Powders Prepared by Spray Pyrolysis Applying Nanoscale Kirkendall Diffusion

Gi Dae Park, Jung Sang Cho, and Yun Chan Kang*

Department of Materials Science and Engineering, Korea University, Seoul 136-713, Republic of Korea

Supporting Information

ABSTRACT: Multicomponent metal oxide hollow-nanosphere decorated reduced graphene oxide (rGO) composite powders are prepared by spray pyrolysis with nanoscale Kirkendall diffusion. The double-layer $NiFe_2O_4$@NiO-hollow-nanosphere decorated rGO composite powders are prepared using the first target material. The NiFe-alloy-nanopowder decorated rGO powders are prepared as an intermediate product by post-treatment under the reducing atmosphere of the $NiFe_2O_4$/NiO-decorated rGO composite powders obtained by spray pyrolysis. The different diffusion rates of Ni (83 pm for Ni^{2+}) and Fe (76 pm for Fe^{2+}, 65 pm for Fe^{3+}) cations with different radii during nanoscale Kirkendall diffusion result in multiphase and double-layer $NiFe_2O_4$@NiO hollow nanospheres. The mean size of the hollow $NiFe_2O_4$@NiO nanospheres decorated uniformly within crumpled rGO is 14 nm. The first discharge capacities of the nanosphere-decorated rGO composite powders with filled $NiFe_2O_4$/NiO and hollow $NiFe_2O_4$@NiO at a current density of 1 A g^{-1} are 1168 and 1319 mA h g^{-1}, respectively. Their discharge capacities for the 100th cycle are 597 and 951 mA h g^{-1}, respectively. The discharge capacity of the $NiFe_2O_4$@NiO-hollow-nanosphere-decorated rGO composite powders at the high current density of 4 A g^{-1} for the 400th cycle is 789 mA h g^{-1}.

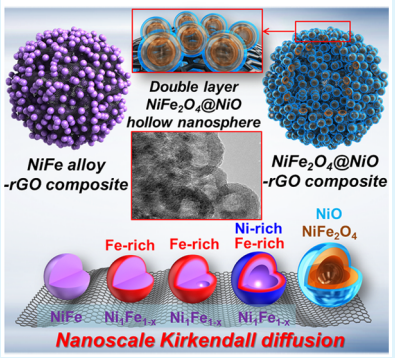

KEYWORDS: *Kirkendall effect, nanostructure, reduced graphene oxide, lithium ion batteries, spray pyrolysis*

INTRODUCTION

High energy density, high rate capability, and long cycle life are essential properties of Li-ion batteries (LIBs) for future electric vehicles and renewable energy storage.[1−10] Various transition-metal oxides have been studied as promising anode materials for rechargeable LIBs because of their high theoretical capacities.[11−18] In particular, multicomponent transition-metal oxides having single and multiple phases have been studied to overcome the poor cycling performance of single-element ones.[19−23]

Nanostructures with different shapes (such as hollow forms, yolk−shell arrangements, and nanotubes) were studied to resolve the issue of volume expansion in metal oxides during cycling. In particular, hollow metal oxide powders used as energy storage materials exhibit good electrochemical properties.[24−29] For example, nanosized hollow metal oxide powders used as energy storage materials exhibit good electrochemical properties at high current densities because of their shortened diffusion length and increased contact area with the electrolyte for Li^+ insertion and extraction.[30−36] Hollow single-component metal oxide powders, with particles a few nanometers in size, have been successfully prepared by nanoscale Kirkendall diffusion using metal nanopowders.[37−44] The difference in the rates of outward diffusion of metal cations through the oxide layer and inward diffusion of oxygen into the metals during the oxidation process results in a hollow metal oxide nanopowder. However, the preparation of multicomponent metal oxide hollow powders, with particles a few nanometers in size, by applying nanoscale Kirkendall diffusion process has been scarcely studied. To the best of our knowledge, the electrochemical properties of the multicomponent metal oxide hollow nanopowders prepared by applying nanoscale Kirkendall diffusion process have not been studied.

Single-component nickel oxide and iron oxide materials showed good electrochemical properties as anode materials for lithium-ion batteries.[55−57] Therefore, in this study, multicomponent metal oxide hollow nanosphere-decorated reduced graphene oxide (rGO) composite powders with a 1:1 Ni/Fe mole ratio are first prepared by spray pyrolysis applying a nanoscale Kirkendall diffusion process. NiFe alloy nanopowder-decorated rGO powders were prepared as an intermediate product by post-treatment under a reducing atmosphere of the $NiFe_2O_4$/NiO-decorated rGO powders obtained by spray pyrolysis. The transformation of NiFe alloy nanopowders into hollow metal oxide nanospheres with the nanoscale Kirkendall diffusion process by post-treatment under air atmosphere resulted in $NiFe_2O_4$@NiO-hollow-nanosphere-decorated rGO composite powders. rGO layers played a key role as a barrier

Received: June 3, 2015
Accepted: July 17, 2015
Published: July 17, 2015

DOI: 10.1021/acsami.5b04891
ACS Appl. Mater. Interfaces 2015, 7, 16842−16849

Scheme 1. Formation Mechanism of the $NiFe_2O_4$@NiO-hollow-nanosphere-decorated rGO Composite Powder by Nanoscale Kirkendall Diffusion

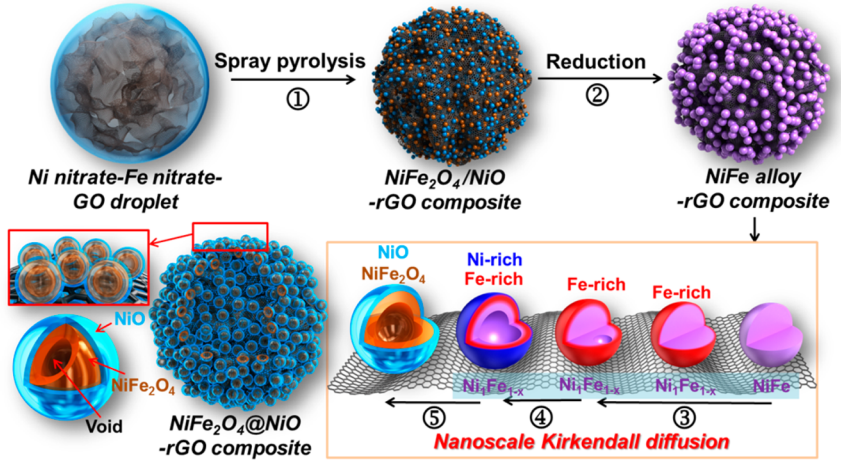

for blocking the growth of NiFe alloy nanopowders and $NiFe_2O_4$@NiO hollow nanospheres during the post-treatment process. rGO layers also provided excellent support to $NiFe_2O_4$@NiO hollow nanospheres because of their high conductivity and flexibility.

RESULTS AND DISCUSSION

The formation mechanism of the $NiFe_2O_4$@NiO-hollow-nanosphere-decorated rGO composite powders with the nanoscale Kirkendall diffusion process in spray pyrolysis is described in Scheme 1. The $NiFe_2O_4$/NiO-decorated rGO composite powder with a 1:1 Ni/Fe molar ratio was prepared directly by spray pyrolysis (Scheme 1-①). The ultrafine NiO and $NiFe_2O_4$ nanocrystals, several nanometers in size, were uniformly distributed over the crumpled rGO structure. The reduction and alloying processes of the $NiFe_2O_4$/NiO nanocrystals under a reducing atmosphere produced the NiFe alloys (Scheme 1-②). The growth of the NiFe alloy nanocrystals was confined by the rGO nanosheets. Therefore, the ultrafine NiFe-alloy-decorated rGO composite powders were prepared by post-treatment of the precursor powders obtained by spray pyrolysis under a reducing atmosphere. The ultrafine NiFe alloy nanocrystals transformed into the hollow $NiFe_2O_4$@NiO nanospheres by the nanoscale Kirkendall diffusion process through an oxidation process under an air atmosphere. In the early oxidation step, NiFe–metal-oxide nanopowder with a core–shell structure was first formed. The Fe (Fe^{2+}, 76 pm; Fe^{3+}, 65 pm) cations with small radii diffused outward more quickly than the inward diffusion of oxygen anions (O^{2-}, 140 pm) to form the Ni_1Fe_{1-x}@metal oxide nanopowder with inter-voids (Scheme 1-③). The iron-rich metal oxide layer was formed during the early stage of the nanoscale Kirkendall diffusion process. The large-radius Ni cations (Ni^{2+}, 83 pm) diffused outward to form the Ni-rich metal oxide layer covering the iron-rich metal oxide layer (Scheme 1-④). The reaction of iron oxide with a partial amount of nickel oxide during the nanoscale Kirkendall diffusion process formed the iron-rich $NiFe_2O_4$ solid solution. The void volume inside of the nanopowder formed by nanoscale Kirkendall diffusion increased with increasing oxidation time. Consequently, the $NiFe_2O_4$/NiO-decorated rGO composite powder prepared by spray pyrolysis transformed into the $NiFe_2O_4$@NiO-hollow-nanosphere-decorated rGO composite powder by this two-step post-treatment process (Scheme 1-⑤).

The morphologies of the $NiFe_2O_4$/NiO-decorated rGO composite powders with a 1:1 Ni/Fe molar ratio prepared by spray pyrolysis are shown in Figure 1. The decomposition of Ni

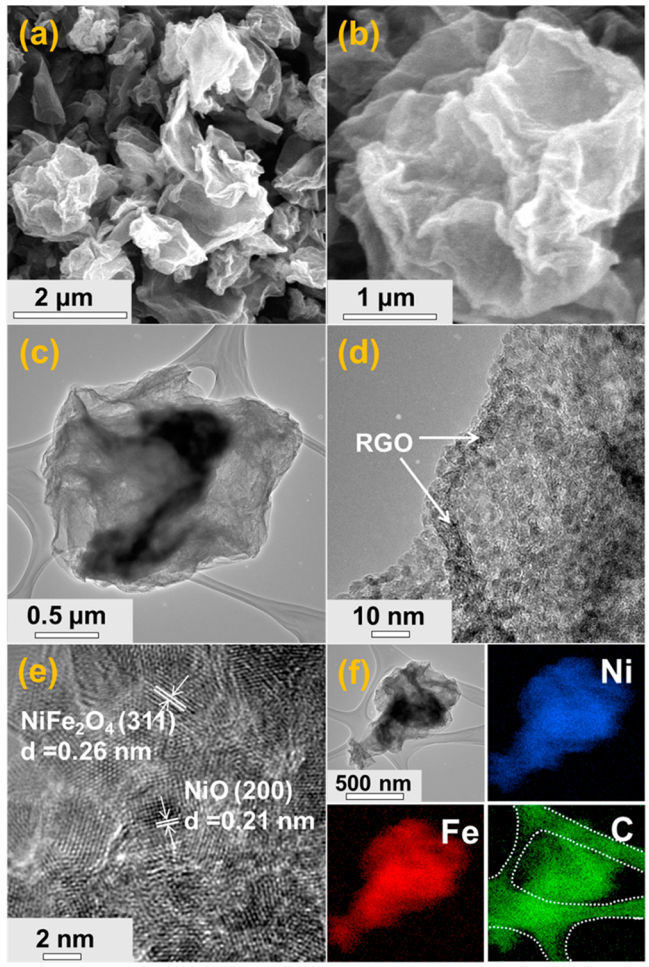

Figure 1. Morphologies and elemental mapping images of $NiFe_2O_4$/NiO-decorated rGO composite powders: (a,b) SEM images, (c,d) TEM images, (e) HR-TEM image, and (f) elemental mapping images.

DOI: 10.1021/acsami.5b04891
ACS Appl. Mater. Interfaces 2015, 7, 16842–16849

and Fe salts and the thermal reduction of GO layers inside the tubular reactor maintained at 500 °C resulted in the formation of $NiFe_2O_4$/NiO-decorated rGO composite powders. The SEM and TEM images show the crumpled structure of the composite powders due to the presence of rGO. The high-resolution TEM image in Figure 1d shows the ultrafine nanocrystals with sizes below 3 nm uniformly dispersed over the rGO layers. The high-resolution TEM image in Figure 1e shows the clear lattice fringes separated by distances of 0.21 and 0.26 nm, which correspond to the (200) and (311) crystal planes of the NiO and $NiFe_2O_4$ phases, respectively. The XRD pattern of the powders directly prepared by spray pyrolysis in Figure S1 shows the mixed crystal structures of the NiO and $NiFe_2O_4$ phases. The elemental mapping images in Figure 1f show the uniform distributions of Ni, Fe, and C components, which are originated from NiO/$NiFe_2O_4$, $NiFe_2O_4$, and rGO, respectively, all over the composite powder.

The powders obtained after post-treatment of the $NiFe_2O_4$/NiO-decorated rGO composite powders at 400 °C under a 10% H_2/Ar atmosphere for 3 h had the crystal structure of the NiFe alloy, as shown in Figure S1 in the Supporting Information. The alloying reaction of Ni and Fe, formed by the reduction of the NiO and $NiFe_2O_4$ nanocrystals, respectively, produced the NiFe-alloy-decorated rGO composite powders. The crumpled structure of the precursor powders was maintained after the reduction process, as shown by the SEM and TEM images in Figures 2a–c. However, the highly aggregated ultrafine $NiFe_2O_4$/NiO nanocrystals transformed into aggregation-free NiFe alloy nanocrystals, as shown by the TEM image in Figure 2d. The high-resolution TEM image in Figure 2e shows the single crystal structure and clear lattice fringes separated by a distance of 0.21 nm, which corresponds to the (111) crystal plane of NiFe alloy. The mean size of the NiFe alloy nanocrystals measured from the high resolution TEM image is 7 nm. The elemental mapping images in Figure 2f show the uniform distributions of Ni, Fe, and C components all over the composite powder. rGO layers protected the crystal growth of NiFe alloys during the reduction process.

The NiFe-alloy-decorated rGO composite powders were post-treated under an air atmosphere at 300 °C for different times to form the $NiFe_2O_4$@NiO-hollow-nanosphere-decorated rGO composite powders. The morphologies of the composite powders obtained after 5 h of oxidation are shown in Figure 3. The $NiFe_2O_4$@NiO hollow nanosphere decorated rGO composite powders obtained after the nanoscale Kirkendall diffusion process have similar overall morphology to those of the $NiFe_2O_4$/NiO- and NiFe alloy-decorated rGO composite powders shown in Figures 1a and 2a. However, the TEM images in Figure 3c,d show that the hollow nanospheres are uniformly dispersed over the rGO layers. The NiFe alloy nanopowders transformed into the hollow $NiFe_2O_4$@NiO nanospheres by the nanoscale Kirkendall diffusion process. The mean size of the hollow $NiFe_2O_4$@NiO nanospheres measured from the high-resolution TEM image shown in Figure 3d is 14 nm. The mean size of the nanopowders is increased twice after void formation by the nanoscale Kirkendall diffusion process. The high-resolution TEM images in Figure 3e show the clear lattice fringes separated by distances of 0.26 and 0.21 nm, which correspond to the (311) and (200) crystal planes of $NiFe_2O_4$ and NiO phases, respectively. The different diffusion rates of Ni (Ni^{2+}, 83 pm) and Fe (Fe^{2+}, 76 pm; Fe^{3+}, 65 pm) cations with different radii resulted in the multiphase and double-layer $NiFe_2O_4$@NiO nanospheres.[45,46] In Figure S1 in

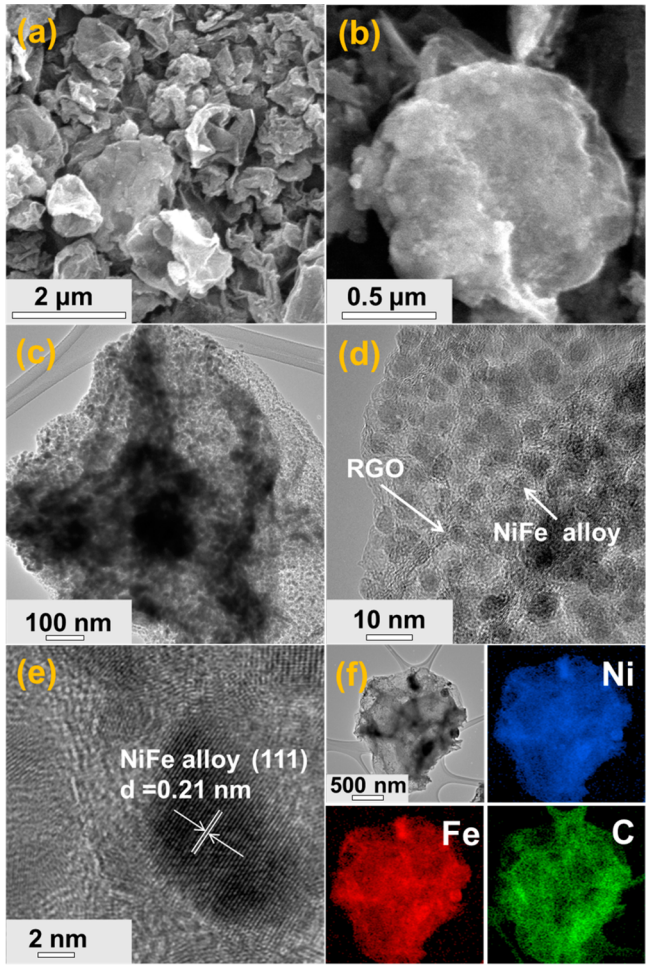

Figure 2. Morphologies and elemental mapping images of NiFe-alloy-decorated rGO composite powders post-treated under a 10% H_2/Ar atmosphere: (a,b) SEM images, (c,d) TEM images, (e) HR-TEM image, and (f) elemental mapping images.

the Supporting Information, the XRD pattern of the powders obtained after the nanoscale Kirkendall diffusion process and directly prepared by spray pyrolysis shows the mixed crystal structure of $NiFe_2O_4$ and NiO phases. The crystalline peaks of NiFe alloy are also observed in the XRD pattern of the powders obtained after the nanoscale Kirkendall diffusion process. However, the XRD pattern has broad peaks due to the ultrafine crystallite size of the nanocrystals consisting of the hollow nanosphere with a shell thickness of 5 nm. The XRD patterns of the powders obtained at different oxidation times of the NiFe-alloy-decorated rGO composite powders were investigated to show the progress of the nanoscale Kirkendall diffusion process with the oxidation time. The crystal peaks of the metal oxide were observed from the XRD pattern of the powders obtained at a short oxidation time of 1 h. However, the peak sharpness of the XRD pattern increased negligibly with the oxidation time, as shown in Figure S2 in the Supporting Information. The elemental mapping images shown in Figure 3f revealed the uniform distribution of Ni, Fe, and C components all over the $NiFe_2O_4$@NiO-hollow-nanosphere-decorated rGO composite powder. The combustion of rGO did not occur during the oxidation process of NiFe alloy by the nanoscale Kirkendall diffusion process to form the $NiFe_2O_4$@NiO-hollow-nanosphere-decorated rGO composite powder. The rGO content of the $NiFe_2O_4$@NiO-nanosphere-decorated

DOI: 10.1021/acsami.5b04891
ACS Appl. Mater. Interfaces 2015, 7, 16842–16849

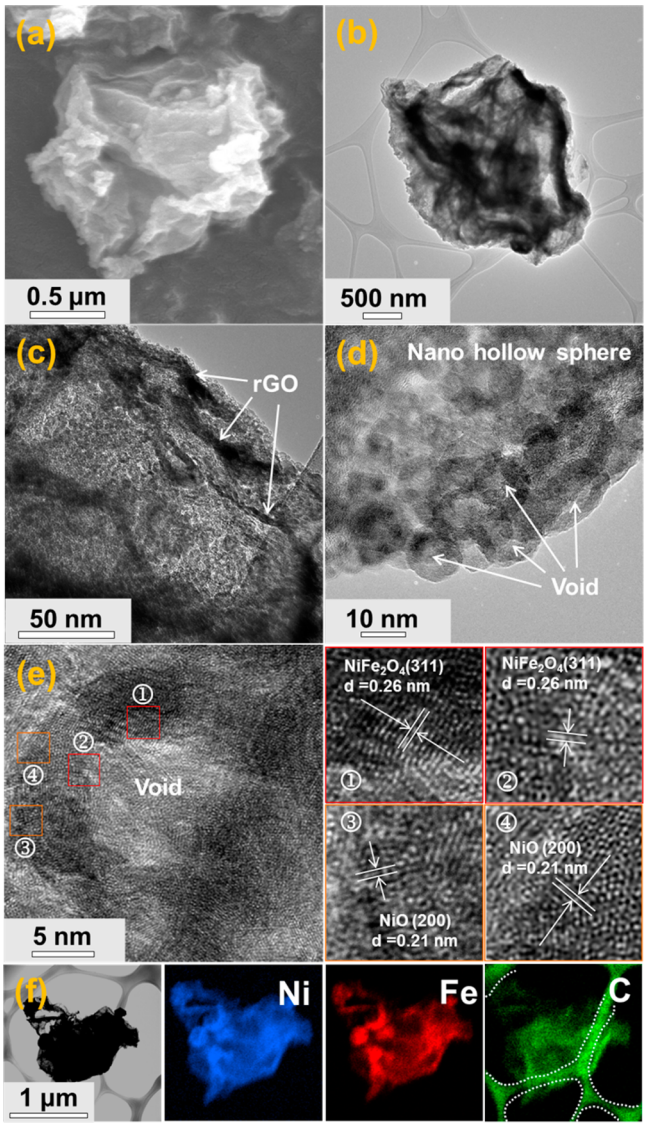

Figure 3. Morphologies and elemental mapping images of $NiFe_2O_4$@NiO hollow-nanosphere-decorated rGO composite powders obtained by nanoscale Kirkendall diffusion: (a) SEM image, (b–d) TEM images, (e) HR-TEM images, and (f) elemental mapping images.

rGO composite powders estimated by TGA shown in Figure S3 in the Supporting Information is 9.0 wt %.

The chemical state and molecular environment of the filled-$NiFe_2O_4$/NiO- and hollow-$NiFe_2O_4$@NiO-nanosphere-decorated rGO composite powders were characterized by XPS. The binding energy patterns associated with Ni 2p in $NiFe_2O_4$/NiO- and $NiFe_2O_4$@NiO-decorated rGO composite powders are similar, as shown in Figure S4a,b in the Supporting Information. The two composite powders have the Ni $2p_{3/2}$ spectrum fitted by considering two spin–orbit doublets characteristic of Ni^{2+} and Ni^{3+} and two shakeup satellites (identified as "Sat"). $NiFe_2O_4$ has shown *n*-type or *p*-type electronic conductivity depending on the different synthesis techniques and crystal sizes. The *p*-type behavior has been attributed to the presence of Ni^{3+} and hole-hopping from Ni^{3+} to Ni^{2+}.[47,48] In the Ni 2p spectrum of $NiFe_2O_4$/NiO-decorated rGO composite powder shown in Figure S4a in the Supporting Information, the main peaks observed at binding energies of 855.9 eV for Ni $2p_{3/2}$ and 873.4 eV for Ni $2p_{1/2}$ are the characteristic Ni^{2+} peaks of NiO and $NiFe_2O_4$.[49−51] The peaks observed at binding energies of 855.9 eV for Ni $2p_{3/2}$ and 873.4 eV for Ni $2p_{1/2}$ are the characteristic peaks of $NiFe_2O_4$. The NiO layer covered the $NiFe_2O_4$ core in the $NiFe_2O_4$@NiO-decorated rGO composite powders. Therefore, the intensity of the peak observed at a binding energy of 855.9 eV for Ni $2p_{3/2}$ of the $NiFe_2O_4$@NiO-decorated rGO composite powders is higher than that of the $NiFe_2O_4$/NiO-decorated rGO composite powders. The Fe 2p spectra shown in Figure S4b,e in the Supporting Information can also be best fitted by considering the two spin–orbit doublets characteristic of Fe^{2+} and Fe^{3+}. The Fe 2p spectra of the two composite powders show two main peaks at binding energies of 711.0 eV for Fe $2p_{3/2}$ and 724.5 eV for Fe $2p_{1/2}$, which are the characteristic peaks of $NiFe_2O_4$.[50−52] In the case of $NiFe_2O_4$/NiO-decorated rGO composite precursor powders, a weak peak is found at 702.8 eV, which can be ascribed to Fe^0. The reducing atmosphere around the powders due to rGO layers during the spray pyrolysis process under an N_2 atmosphere resulted in the partial reduction of the Fe component into iron metal. The C 1s peaks shown in Figure S4c,f in the Supporting Information can be attributed to sp^2-bonded carbon (C–C), epoxy and alkoxy groups (C–O), and carbonyl and carboxylic (C═O) groups, which correspond to peaks at 284.9, 286.7, and 287.6 eV, respectively. The sharp XPS peaks at 284.6 eV indicate the thermal reduction of GO into rGO for both the filled-$NiFe_2O_4$/NiO- and the hollow-$NiFe_2O_4$@NiO-nanosphere-decorated rGO composite powders.[53,54] The BET surface areas of the filled-$NiFe_2O_4$/NiO- and hollow-$NiFe_2O_4$@NiO-nanosphere-decorated rGO composite powders are 121.8 and 113.4 $m^2\ g^{-1}$, respectively. The ultrafine NiO and $NiFe_2O_4$ nanocrystals transformed into the large-size $NiFe_2O_4$@NiO hollow nanosphere having a gas-impermeable shell after the second-step post-treatment process. Therefore, the $NiFe_2O_4$/NiO-decorated rGO composite powder prepared directly by spray pyrolysis had a higher BET surface area than that of the $NiFe_2O_4$@NiO-hollow-nanosphere-decorated rGO composite powder.

The CVs of the filled-$NiFe_2O_4$/NiO- and hollow-$NiFe_2O_4$@NiO-nanosphere-decorated rGO composite powders during the first five cycles at a scan rate of 0.07 mV s^{-1} in the voltage range of 0.001–3 V are shown in Figure 4a,b. The first cathodic scan of the $NiFe_2O_4$/NiO-decorated rGO composite powders shows two peaks located at 1.2 and 0.7 V, which can be attributed to Li insertion into the structure and the reduction of Fe^{3+} and Ni^{2+} to Fe^0 and Ni^0, respectively, and the formation of amorphous Li_2O.[55−58] The clear reduction peak at around 1.2 V has been rarely observed in the first cathodic scan of the $NiFe_2O_4$@NiO-hollow-nanosphere-decorated rGO composite powders. The two broad oxidation peaks observed at around 1.5 and 2.3 V in the first charging process of the two composite powders are attributed to the oxidation of Ni^0 to Ni^{2+} and of Fe^0 to Fe^{2+} and Fe^{3+}.[55−58] From the second cycle onward, the cathodic and anodic peaks in the CV tests overlapped substantially, indicating that the electrodes of the two composite powders have outstanding cycle ability for the insertion and desertion of Li ions.

The initial discharge and charge curves of the filled-$NiFe_2O_4$/NiO- and hollow-$NiFe_2O_4$@NiO-nanosphere-decorated rGO composite powders at a current density of 1 A g^{-1} are shown in Figure 4c. The first discharge capacities of the filled-$NiFe_2O_4$/NiO- and hollow-$NiFe_2O_4$@NiO-nanosphere-decorated rGO composite powders are 1168 and 1319 mA h g^{-1}, respectively,

DOI: 10.1021/acsami.5b04891
ACS Appl. Mater. Interfaces 2015, 7, 16842–16849

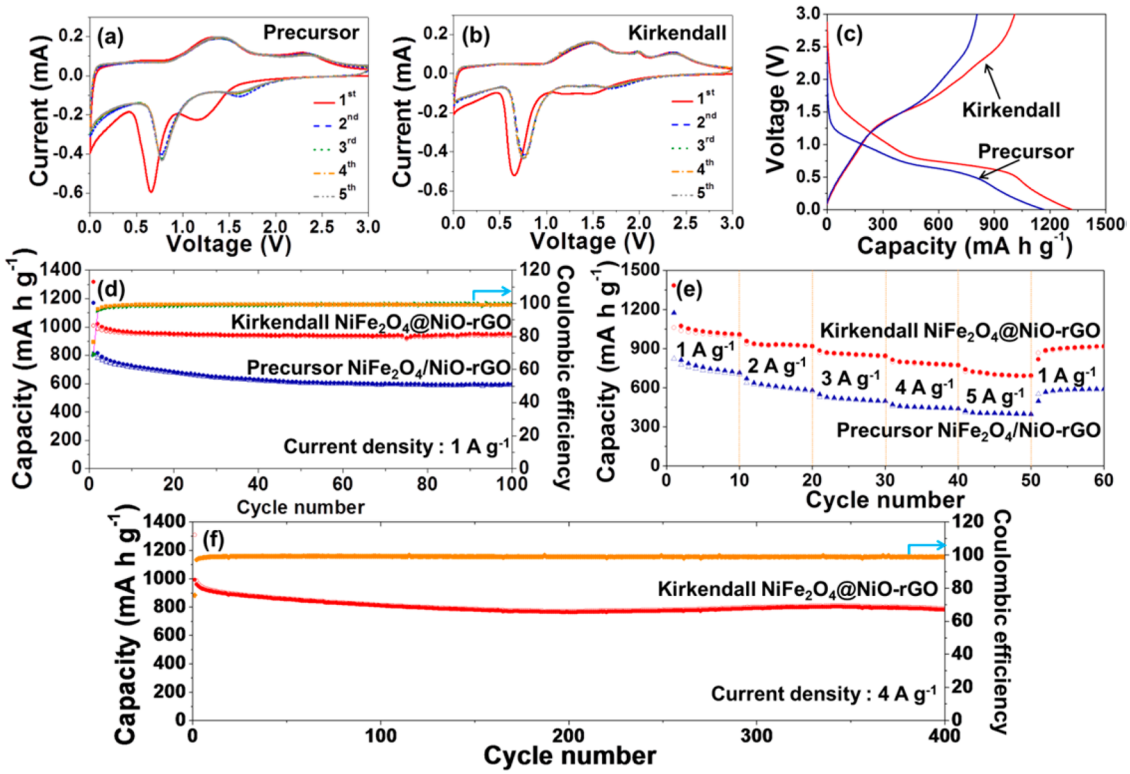

Figure 4. Electrochemical properties of filled-$NiFe_2O_4$/NiO- and hollow-$NiFe_2O_4$@NiO-nanosphere-decorated rGO composite powders: (a,b) CV curves, (c) initial charge−discharge curves, (d) cycling performances and Coulombic efficiencies, (e) rate performances, and (f) long cycling performance and Coulombic efficiencies.

and their initial Coulombic efficiencies are 69% and 77%. The cycling performances of the two samples at a current density of 1 A g^{-1} are shown in Figure 4d. The capacity fadings of the filled-$NiFe_2O_4$/NiO- and hollow-$NiFe_2O_4$@NiO-nanosphere-decorated rGO composite powders are observed during the initial 50 and 10 cycles, respectively. The electrochemical grinding effect during cycling led to the partial structural destruction of the powders and provoked capacity fading during the initial 10 cycles of the $NiFe_2O_4$@NiO-hollow-nanosphere-decorated rGO composite powders.[59,60] The continuous capacity fading of the $NiFe_2O_4$/NiO-decorated rGO composite powders during the further 40 cycles revealed the structural instability during repeated lithium insertion and desertion processes. The discharge capacities of the $NiFe_2O_4$@NiO-hollow-nanosphere-decorated rGO composite powders increase slightly from the 22nd cycle up to 951 mA h g^{-1} for the 100th cycle due to the formation of a polymeric gel-like film on the active material.[61,62] The discharge capacity of the filled-$NiFe_2O_4$/NiO-decorated rGO composite powders for the 100th cycle is 597 mA h g^{-1}. The rate performances of the two composite powders are shown in Figure 4e, in which the current density is increased stepwise from 1 to 5 A g^{-1} with a step size of 1 A g^{-1}. The filled-$NiFe_2O_4$/NiO- and hollow-$NiFe_2O_4$@NiO-nanosphere-decorated rGO composite powders had final discharge capacities of 716, 581, 498, 441, and 399 mA h g^{-1} and 1008, 920, 844, 773, and 694 mA h g^{-1} at current densities of 1, 2, 3, 4, and 5 A g^{-1}, respectively. The long-term cycling performance and Coulombic efficiencies of the $NiFe_2O_4$@NiO-hollow-nanosphere-decorated rGO composite powders at the high current density of 4 A g^{-1} are shown in Figure 4f. The discharge capacities of the composite powders for the first and 400th cycles were 1308 and 789 mA h g^{-1}, respectively, and their capacity retention measured from the second cycle is 80%. The hollow-$NiFe_2O_4$@NiO-nanosphere-decorated rGO composite powders showed high Coulombic efficiencies of above 99.0% from the 10th cycle onward at high current densities of 1 and 4 A g^{-1} as shown in Figure 4 parts d and f, respectively. The impedance measurements of the composite powders were carried out at room temperature before and after 1 and 100 cycles at a current density of 1 A g^{-1}. Electrochemical impedance spectroscopy of the $NiFe_2O_4$@NiO-hollow-nanosphere-decorated rGO composite powders was conducted to evaluate their electrochemical properties. The resulting Nyquist plots in Figure S5 in the Supporting Information show semicircles in the medium-frequency range that are assigned to the charge-transfer resistance of the electrodes. The charge-transfer resistance of the composite powders decreased after cycling due to the transformation of the crystalline structure into an amorphous structure after the first cycle. The charge-transfer resistances of the $NiFe_2O_4$@NiO-hollow-nanosphere-decorated rGO composite powders with high structural stability during repeated lithium insertion and desertion processes increased slightly during the 100 cycles. The morphologies of the $NiFe_2O_4$@NiO-hollow-nanosphere-decorated rGO composite powders obtained after 100 cycles at a current density of 2 A g^{-1} are shown in Figure S6 in the Supporting Information. The hollow structure of the nanospheres consisting of the composite powder was well-maintained even after repeated lithium insertion and desertion processes.

CONCLUSIONS

Multicomponent $NiFe_2O_4$@NiO-hollow-nanosphere-decorated rGO composite powders were prepared by spray pyrolysis

DOI: 10.1021/acsami.5b04891
ACS Appl. Mater. Interfaces 2015, 7, 16842−16849

applying nanoscale Kirkendall diffusion process. The filled-$NiFe_2O_4$/NiO-decorated rGO composite powders prepared by one-pot spray pyrolysis transformed into the $NiFe_2O_4$@NiO-hollow-nanosphere-decorated rGO composite powders by a two-step post-treatment process under reducing and oxidating conditions. rGO layers played a key role as a barrier for blocking the growth of NiFe alloy nanopowders and $NiFe_2O_4$@NiO hollow nanospheres during the post-treatment process. To conclude, the crumpled rGO powders uniformly decorated with ultrafine $NiFe_2O_4$@NiO hollow nanospheres, showing superior cycling and rate performances for lithium ion storage, were successfully prepared. This simple process can be successfully applied in the preparation of multicomponent hollow metal oxide nanosphere-decorated rGO composite powders with different compositions for a variety of applications including energy storage.

EXPERIMENTAL SECTION

Sample Preparation. A three-step process was applied to the preparation of $NiFe_2O_4$@NiO-hollow-nanosphere-decorated rGO composite powders. The $NiFe_2O_4$/NiO-decorated rGO composite powders were prepared by a simple spray pyrolysis process using a spray solution of nickel nitrate hexahydrate ($Ni(NO_3)_2{\cdot}6H_2O$), iron nitrate nonahydrate ($Fe(NO_3)_3{\cdot}9H_2O$), and graphene oxide (GO) nanosheets. GO nanosheets were synthesized from graphite flakes using a modified Hummers method, as described in our previous report.[55] As-synthesized GO nanosheets were redispersed in distilled water and then exfoliated by ultrasonication. Samples containing 0.015 M of $Ni(NO_3)_2{\cdot}6H_2O$ and 0.015 M of $Fe(NO_3)_3{\cdot}9H_2O$ were dissolved in 500 mL of 1 mg mL^{-1} exfoliated GO dispersion to fabricate the $NiFe_2O_4$/NiO-decorated rGO composite powders. In the spray pyrolysis process, droplets were generated using a 1.7-MHz ultrasonic spray generator consisting of six vibrators. The droplets were carried to a quartz reactor with a length of 1200 mm and a diameter of 50 mm using N_2 as the carrier gas at a flow rate of 10 L min^{-1}. The reactor temperature was maintained at 500 °C. The first step in the post-treatment process was carried out at 400 °C for 3 h under a 10% H_2/Ar reducing atmosphere; this produced NiFe-alloy-decorated rGO composite powders. The second step in the post-treatment process of the NiFe-alloy-decorated rGO composite powders was carried out at 300 °C for 5 h in air atmosphere to produce $NiFe_2O_4$@NiO-hollow-nanosphere-decorated rGO composite powders.

Characterization. The crystal structures of the powders were investigated using X-ray diffractometry (XRD, X'pert PRO MPD) with Cu−K_α radiation (λ = 1.5418 Å) at the Korea Basic Science Institute (Daegu, Korea). The morphologies of the powders were investigated using field-emission scanning electron microscopy (FE-SEM, Hitachi S-4800) and high-resolution transmission electron microscopy (HR-TEM, JEOL JEM-2100F) at a working voltage of 200 kV. The specific surface areas of the powders before and after post-treatment at various temperatures were calculated by a Brunauer−Emmett−Teller (BET) analysis of nitrogen-adsorption measurements (TriStar 3000). The X-ray photoelectron spectroscopy (XPS) of the powders was performed using ESCALAB-250 with Al Kα radiation (1486.6 eV). To determine the amount of reduced graphene oxide in the $NiFe_2O_4$@NiO-hollow-nanosphere-decorated rGO composite powder, we performed a thermogravimetric analysis (TGA, SDT Q600) in air at a heating rate of 10 °C min^{-1}.

Electrochemical Measurements. The electrochemical properties of the powder were analyzed using a 2032-type coin cell. The anode was prepared by mixing the active material, carbon black, and sodium carboxymethyl cellulose in a weight ratio of 7:2:1. Li metal and microporous polypropylene film were used as the counter electrode and the separator, respectively. The electrolyte was 1 M $LiPF_6$ dissolved in a mixture of fluoroethylene carbonate−dimethyl carbonate (FEC/DMC; 1:1 v/v). The discharge and charge characteristics of the samples were investigated by cycling in the potential range of 0.001−3 V at various current densities. Cyclic voltammograms (CVs) were measured at a scan rate of 0.07 mV s^{-1}.

ASSOCIATED CONTENT

Supporting Information

Figures showing the XRD patterns of the filled-$NiFe_2O_4$/NiO-, NiFe-alloy-, and hollow-$NiFe_2O_4$@NiO-nanosphere-decorated rGO composite powders; XRD patterns of the powders obtained at different oxidation times of the NiFe alloy-decorated rGO composite powders; the TG curve of the $NiFe_2O_4$@NiO-hollow-nanosphere-decorated rGO composite powders; the XPS spectra of the filled-$NiFe_2O_4$/NiO-, and hollow-$NiFe_2O_4$@NiO-nanosphere-decorated rGO composite powders; the electrochemical impedance spectroscopy (EIS) of the $NiFe_2O_4$@NiO-hollow-nanosphere-decorated rGO composite powders before and after cycling; morphologies of the $NiFe_2O_4$@NiO-hollow-nanosphere-decorated rGO composite powders obtained after 100 cycles; cycling performance of the hollow-$NiFe_2O_4$@NiO-nanosphere-decorated rGO composite powders; and the N_2 adsorption and desorption isotherms of the filled-$NiFe_2O_4$/NiO- and hollow-$NiFe_2O_4$@NiO-nanosphere-decorated rGO composite powders. The Supporting Information is available free of charge on the ACS Publications website at DOI: 10.1021/acsami.5b04891.

AUTHOR INFORMATION

Corresponding Author

*E-mail: yckang@korea.ac.kr. Fax: (+82) 2-928-3584.

Notes

The authors declare no competing financial interest.

ACKNOWLEDGMENTS

This work was supported by the Energy Efficiency and Resources Core Technology Program of the Korea Institute of Energy Technology Evaluation and Planning (KETEP) and was granted financial resources from the Ministry of Trade, Industry and Energy, Republic of Korea (201320200000420).

REFERENCES

(1) Gogotsi, Y. What Nano Can Do for Energy Storage. *ACS Nano* **2014**, *8*, 5369−5371.

(2) Dunn, B.; Kamath, H.; Tarascon, J. M. Electrical Energy Storage for the Grid: A Battery of Choices. *Science* **2011**, *334*, 928−935.

(3) Liu, N.; Lu, Z.; Zhao, J.; McDowell, M. T.; Lee, H. W.; Zhao, W.; Cui, Y. A Pomegranate-inspired Nanoscale Design for Large-Volume-Change Lithium Battery Anodes. *Nat. Nanotechnol.* **2014**, *9*, 187−192.

(4) Lou, X. W.; Li, C. M.; Archer, L. A. Designed Synthesis of Coaxial SnO_2@carbon Hollow Nanospheres for Highly Reversible Lithium Storage. *Adv. Mater.* **2009**, *21*, 2536−2539.

(5) Liu, C.; Li, F.; Ma, L. P.; Cheng, H. M. Advanced Materials for Energy Storage. *Adv. Mater.* **2010**, *22*, E28−E62.

(6) Liu, N.; Wu, H.; McDowell, M. T.; Yao, Y.; Wang, C. M.; Cui, Y. A Yolk-Shell Design for Stabilized and Scalable Li-Ion Battery Alloy Anodes. *Nano Lett.* **2012**, *12*, 3315−3321.

(7) Larcher, D.; Tarascon, J. M. Towards Greener and More Sustainable Batteries for Electrical Energy Storage. *Nat. Chem.* **2014**, *7*, 19−29.

(8) Wang, D. H.; Choi, D. W.; Li, J.; Yang, Z. G.; Nie, Z. M.; Kou, R.; Hu, D. H.; Wang, C. M.; Saraf, L. V.; Zhang, J. G.; Aksay, I. H. A.; Liu, J. Self-Assembled TiO_2−Graphene Hybrid Nanostructures for Enhanced Li-Ion Insertion. *ACS Nano* **2009**, *3*, 907−914.

(9) Cheng, Y. W.; Parent, L. R.; Shao, Y. Y.; Wang, C. M.; Sprenkle, V. L.; Li, G. S.; Liu, J. Facile Synthesis of Chevrel Phase Nanocubes and Their Applications for Multivalent Energy Storage. *Chem. Mater.* **2014**, *26*, 4904−4907.

DOI: 10.1021/acsami.5b04891
ACS Appl. Mater. Interfaces 2015, 7, 16842−16849

(10) Li, X. L.; Gu, M.; Hu, S. Y.; Kennard, R.; Yan, P. F.; Chen, X.; Wang, C. M.; Sailor, M. J.; Zhang, J. G.; Liu, J. Mesoporous Silicon Sponge as an Anti-Pulverization Structure for High-Performance Lithium-ion Battery Anodes. *Nat. Commun.* **2014**, *5*, 4105.
(11) Poizot, P.; Laruelle, S.; Grugeon, S.; Dupont, L.; Tarascon, J. M. Nano-sized Transition-Metal Oxides as Negative-Electrode Materials for Lithium-ion Batteries. *Nature* **2000**, *407*, 496−499.
(12) Reddy, M. V.; Rao, G. V. S.; Chowdari, B. V. R. Metal Oxides and Oxysalts as Anode Materials for Li Ion Batteries. *Chem. Rev.* **2013**, *113*, 5364−5457.
(13) Jiang, J.; Li, Y. Y.; Liu, J. P.; Huang, X. T.; Yuan, C. Z.; Lou, X. W. Recent Advances in Metal Oxide-based Electrode Architecture Design for Electrochemical Energy Storage. *Adv. Mater.* **2012**, *24*, 5166−5180.
(14) Sun, X. L.; Yan, C. L.; Chen, Y.; Si, W. P.; Deng, J. W.; Oswald, S.; Liu, L. F.; Schmidt, O. G. Three-Dimensionally "Curved" NiO Nanomembranes as Ultrahigh Rate Capability Anodes for Li-Ion Batteries with Long Cycle Lifetimes. *Adv. Energy Mater.* **2014**, *4*, 1300912.
(15) Zhang, L.; Wu, H. B.; Lou, X. W. Iron-Oxide-Based Advanced Anode Materials for Lithium-Ion Batteries. *Adv. Energy Mater.* **2014**, *4*, 1300958.
(16) Lin, J.; Raji, A. R. O.; Nan, K. W.; Peng, Z. W.; Yan, Z.; Samuel, E. L. G.; Natelson, D.; Tour, J. M. Iron Oxide Nanoparticle and Graphene Nanoribbon Composite as an Anode Material for High-Performance Li-Ion Batteries. *Adv. Funct. Mater.* **2014**, *24*, 2044−2048.
(17) Rahman, M. M.; Wang, J. Z.; Deng, X. L.; Li, Y.; Liu, H. K. Hydrothermal Synthesis of Nanostructured Co_3O_4 Materials under Pulsed Magnetic Field and with an Aging Technique, and Their Electrochemical Performance as Anode for Lithium-Ion Battery. *Electrochim. Acta* **2009**, *55*, 504−510.
(18) Jiang, H.; Hu, Y. J.; Guo, S. J.; Yan, C. Y.; Lee, P. S.; Li, C. Z. Rational Design of MnO/Carbon Nanopeapods with Internal Void Space for High-Rate and Long-Life Li-Ion Batteries. *ACS Nano* **2014**, *8*, 6038−6046.
(19) Gao, G. X.; Wu, H. B.; Lou, X. W. Citrate-Assisted Growth of $NiCo_2O_4$ Nanosheets on Reduced Graphene Oxide for Highly Reversible Lithium Storage. *Adv. Energy Mater.* **2014**, *4*, 1400422.
(20) Li, S.; Li, A.; Zhang, R.; He, Y. Y.; Zhai, Y. J.; Xu, L. Q. Hierarchical Porous Metal Ferrite Ball-In-Ball Hollow Spheres: General Synthesis, Formation Mechanism, and High Performance as Anode Materials for Li-Ion Batteries. *Nano Res.* **2014**, *7*, 1116−1127.
(21) Hou, L. R.; Lian, L.; Zhang, L. H.; Pang, G.; Yuan, C. Z.; Zhang, X. G. Self-Sacrifice Template Fabrication of Hierarchical Mesoporous Bi-Component-Active ZnO/$ZnFe_2O_4$ Sub- Microcubes as Superior Anode Towards High-Performance Lithium-Ion Battery. *Adv. Funct. Mater.* **2015**, *25*, 238−246.
(22) Huang, G.; Zhang, F. F.; Du, X. C.; Wang, J. W.; Yin, D. M.; Wang, L. M. Core−Shell $NiFe_2O_4$@TiO_2 Nanorods: An Anode Material with Enhanced Electrochemical Performance for Lithium-Ion Batteries. *Chem. - Eur. J.* **2014**, *20*, 11214−11219.
(23) Cherian, C. T.; Sundaramurthy, J.; Reddy, M. V.; Kumar, P. S.; Mani, K.; Pliszka, D.; Sow, C. H.; Ramakrishna, S.; Chowdari, B. V. R. Morphologically Robust $NiFe_2O_4$ Nanofibers as High Capacity Li-Ion Battery Anode Material. *ACS Appl. Mater. Interfaces* **2013**, *5*, 9957−9963.
(24) Zhang, G. Q.; Lou, X. W. General Synthesis of Multi-Shelled Mixed Metal Oxide Hollow Spheres with Superior Lithium Storage Properties. *Angew. Chem.* **2014**, *126*, 9187−9190.
(25) Zhang, H. W.; Zhou, L.; Noonan, O.; Martin, D. J.; Whittaker, A. K.; Yu, C. Z. Tailoring the Void Size of Iron Oxide@Carbon Yolk−Shell Structure for Optimized Lithium Storage. *Adv. Funct. Mater.* **2014**, *24*, 4337−4342.
(26) Shen, L. F.; Yu, L.; Yu, X. Y.; Zhang, X. G.; Lou, X. W. Self-Templated Formation of Uniform $NiCo_2O_4$ Hollow Spheres with Complex Interior Structures for Lithium-Ion Batteries and Supercapacitors. *Angew. Chem., Int. Ed.* **2015**, *54*, 1868−1872.
(27) Hong, Y. J.; Son, M. Y.; Kang, Y. C. One-Pot Facile Synthesis of Double-Shelled SnO_2 Yolk-Shell-Structured Powders by Continuous Process as Anode Materials for Li-ion Batteries. *Adv. Mater.* **2013**, *25*, 2279−2283.
(28) Hong, Y. J.; Yoon, J. W.; Lee, J. H.; Kang, Y. C. A New Concept for Obtaining SnO_2 Fiber-in-Tube Nanostructures with Superior Electrochemical Properties. *Chem. - Eur. J.* **2015**, *21*, 371−376.
(29) Park, G. D.; Lee, J. H.; Lee, J. K.; Kang, Y. C. Effect of Esterification Reaction of Citric Acid and Ethylene Glycol on the Formation of Multi-Shelled Cobalt Oxide Powders with Superior Electrochemical Properties. *Nano Res.* **2014**, *7*, 1738−1748.
(30) Park, J. C.; Kim, J. H.; Kwon, H. S.; Song, H. J. Gram-Scale Synthesis of Cu_2O Nanocubes and Subsequent Oxidation to CuO Hollow Nanostructures for Lithium-Ion Battery Anode Materials. *Adv. Mater.* **2009**, *21*, 803−807.
(31) Koo, B.; Xiong, H.; Slater, M. D.; Prakapenka, V. B.; Balasubramanian, M.; Podsiadlo, P.; Johnson, C. S.; Rajh, T.; Shevchenko, E. V. Hollow Iron Oxide Nanoparticles for Application in Lithium Ion Batteries. *Nano Lett.* **2012**, *12*, 2429−2435.
(32) Wang, Z. Y.; Luan, D. Y.; Boey, F. Y. C.; Lou, X. W. Fast Formation of SnO_2 Nanoboxes with Enhanced Lithium Storage Capability. *J. Am. Chem. Soc.* **2011**, *133*, 4738−4741.
(33) Zhang, G. Q.; Wu, H. B.; Song, T. S.; Paik, U. G.; Lou, X. W. TiO_2 Hollow Spheres Composed of Highly Crystalline Nanocrystals Exhibit Superior Lithium Storage Properties. *Angew. Chem., Int. Ed.* **2014**, *53*, 12590−12593.
(34) Guo, H.; Li, T. T.; Chen, W. W.; Liu, L. X.; Yang, X. J.; Wang, Y. P.; Guo, Y. C. General Design of Hollow Porous $CoFe_2O_4$ Nanocubes from Metal−Organic Frameworks with Extraordinary Lithium Storage. *Nanoscale* **2014**, *6*, 15168−15174.
(35) Kim, W. S.; Hwa, Y.; Kim, H. C.; Choi, J. H.; Sohn, H. J.; Hong, S. H. SnO_2@Co_3O_4 Hollow Nano-spheres for a Li ion Battery Anode with Extraordinary Performance. *Nano Res.* **2014**, *7*, 1128−1136.
(36) Sasidharan, M.; Gunawardhana, N.; Senthil, C.; Yoshio, M. Micelle Templated NiO Hollow Nanospheres as Anode Materials in Lithium Ion Batteries. *J. Mater. Chem. A* **2014**, *2*, 7337−7344.
(37) Cho, J. S.; Hong, Y. J.; Kang, Y. C. Design and Synthesis of Bubble-Nanorod-Structured Fe_2O_3-Carbon Nanofibers as Advanced Anode Material for Li-Ion Batteries. *ACS Nano* **2015**, *9*, 4026−4035.
(38) Yin, Y. D.; Rioux, R. M.; Erdonmez, C. K.; Hughes, S.; Somorjai, G. A.; Alivisatos, A. P. Formation of Hollow Nanocrystals Through the Nanoscale Kirkendall Effect. *Science* **2004**, *304*, 711−714.
(39) Anderson, B. D.; Tracy, J. B. Nanoparticle Conversion Chemistry: Kirkendall Effect, Galvanic Exchange, and Anion Exchange. *Nanoscale* **2014**, *6*, 12195−12216.
(40) Railsback, J. G.; Johnston-Peck, A. C.; Wang, J. W.; Tracy, J. B. Size-Dependent Nanoscale Kirkendall Effect During the Oxidation of Nickel Nanoparticles. *ACS Nano* **2010**, *4*, 1913−1920.
(41) Fan, H. J.; Knez, M.; Scholz, R.; Hesse, D.; Nielsch, K.; Zacharias, M.; Gosele, U. Influence of Surface Diffusion on the Formation of Hollow Nanostructures Induced by the Kirkendall Effect: The Basic Concept. *Nano Lett.* **2007**, *7*, 993−997.
(42) Hu, L.; Yan, N.; Chen, Q. W.; Zhang, P.; Zhong, H.; Zheng, X. R.; Li, Y.; Hu, X. Y. Fabrication Based on the Kirkendall Effect of Co_3O_4 Porous Nanocages with Extraordinarily High Capacity for Lithium Storage. *Chem. - Eur. J.* **2012**, *18*, 8971−8977.
(43) Fan, H. J.; Gösele, U.; Zacharias, M. Formation of Nanotubes and Hollow Nanoparticles Based on Kirkendall and Diffusion Processes: A Review. *Small* **2007**, *3*, 1660−1671.
(44) Lee, Y. M.; Jo, M. R.; Song, K. S.; Nam, K. M.; Park, J. T.; Kang, Y. M. Hollow Sn−SnO_2 Nanocrystal/Graphite Composites and Their Lithium Storage Properties. *ACS Appl. Mater. Interfaces* **2012**, *4*, 3459−3464.
(45) Wang, C. M.; Genc, A.; Cheng, H. K.; Pullan, L.; Baer, D. R.; Bruemmer, S. M. In-Situ TEM Visualization of Vacancy Injection and Chemical Partition During Oxidation of Ni-Cr Nanoparticles. *Sci. Rep.* **2014**, *4*, 3683.
(46) Fan, H. J.; Knez, M.; Scholz, R.; Nielsch, K.; Pippel, E.; Hesse, D.; Gösele, U.; Zacharias, M. Single-Crystalline $MgAl_2O_4$ Spinel Nanotubes Using a Reactive and Removable MgO Nanowire Template. *Nanotechnology* **2006**, *17*, 5157−5162.

DOI: 10.1021/acsami.5b04891
ACS Appl. Mater. Interfaces 2015, 7, 16842−16849

(47) Solís, C.; Somacescu, S.; Palafox, E.; Balaguer, M.; Serra, J. M. Particular Transport Properties of $NiFe_2O_4$ Thin Films at High Temperatures. *J. Phys. Chem. C* **2014**, *118*, 24266−24273.
(48) Sutka, A.; Pärna, R.; Mezinskis, G.; Kisand, V. Effects of Co Ion Addition and Annealing Conditions on Nickel Ferrite Gas Response. *Sens. Actuators, B* **2014**, *192*, 173−180.
(49) Chen, L. Y.; Dai, H.; Shen, Y. M.; Bai, J. F. Size-Controlled Synthesis and Magnetic Properties of $NiFe_2O_4$ Hollow Nanospheres via a Gel-Assistant Hydrothermal Route. *J. Alloys Compd.* **2010**, *491*, L33−L38.
(50) Heidari, E. K.; Zhang, B.; Sohi, M. H.; Ataie, A.; Kim, J. K. Sandwich-Structured Graphene−$NiFe_2O_4$−Carbon Nanocomposite Anodes with Exceptional Electrochemical Performance for Li Ion Batteries. *J. Mater. Chem. A* **2014**, *2*, 8314−8322.
(51) Fu, M.; Jiao, Q. Z.; Zhao, Y. Preparation of $NiFe_2O_4$ Nanorod−Graphene Composites via an Ionic Liquid Assisted One-Step Hydrothermal Approach and Their Microwave Absorbing Properties. *J. Mater. Chem. A* **2013**, *1*, 5577−5586.
(52) Feng, S. J.; Yang, W.; Wang, Z. B. Synthesis of Porous $NiFe_2O_4$ Microparticles and its Catalytic Properties for Methane Combustion. *Mater. Sci. Eng., B* **2011**, *176*, 1509−1512.
(53) Maiti, U. N.; Lim, J. W.; Lee, K. E.; Lee, W. J.; Kim, S. O. Three-Dimensional Shape Engineered, Interfacial Gelation of Reduced Graphene Oxide for High Rate, Large Capacity Supercapacitors. *Adv. Mater.* **2014**, *26*, 615−619.
(54) Choi, S. H.; Kang, Y. C. Synergetic Compositional and Morphological Effects for Improved Na^+ Storage Properties of $Ni_3Co_6S_8$-Reduced Graphene Oxide Composite Powders. *Nanoscale* **2015**, *7*, 6230−6237.
(55) Choi, S. H.; Kang, Y. C. Fe_3O_4-Decorated Hollow Graphene Balls Prepared by Spray Pyrolysis Process for Ultrafast and Long Cycle-Life Lithium Ion Batteries. *Carbon* **2014**, *79*, 58−66.
(56) Zhou, G. M.; Wang, D. W.; Hou, P. X.; Li, W. S.; Li, N.; Liu, C.; Li, F.; Cheng, H. M. A Nanosized Fe_2O_3 Decorated Single-Walled Carbon Nanotube Membrane as a High-Performance Flexible Anode for Lithium Ion Batteries. *J. Mater. Chem.* **2012**, *22*, 17942−17946.
(57) Choi, S. H.; Kang, Y. C. Ultrafast Synthesis of Yolk-Shell and Cubic NiO Nanopowders and Application in Lithium Ion Batteries. *ACS Appl. Mater. Interfaces* **2014**, *6*, 2312−2316.
(58) Huang, G.; Zhang, F. F.; Zhang, L. L.; Du, X. C.; Wang, J. W.; Wang, L. M. Hierarchical $NiFe_2O_4/Fe_2O_3$ Nanotubes Derived from Metal Organic Frameworks for Superior Lithium Ion Battery Anodes. *J. Mater. Chem. A* **2014**, *2*, 8048−8053.
(59) Wang, J. J.; Zhou, H.; Nanda, J. J.; Braun, P. V. Three-Dimensionally Mesostructured Fe_2O_3 Electrodes with Good Rate Performance and Reduced Voltage Hysteresis. *Chem. Mater.* **2015**, *27*, 2803.
(60) Dong, Y. C.; Yung, K. C.; Ma, R. G.; Yang, X.; Chui, Y. S.; Lee, J. M.; Zapien, J. A. Graphene/Acid Assisted Facile Synthesis of Structure-Tuned Fe_3O_4 and Graphene Composites as Anode Materials for Lithium Ion Batteries. *Carbon* **2015**, *86*, 310−317.
(61) Bai, J.; Li, X. G.; Liu, G. Z.; Qian, Y. T.; Xiong, S. L. Unusual Formation of $ZnCo_2O_4$ 3D Hierarchical Twin Microspheres as a High-Rate and Ultralong-Life Lithium-Ion Battery Anode Material. *Adv. Funct. Mater.* **2014**, *24*, 3012−3020.
(62) Jiang, Y. Z.; Zhang, D.; Li, Y.; Yuan, T.; Bahlawane, N.; Liang, C.; Sun, W. P.; Lu, Y. H.; Yan, M. Amorphous Fe_2O_3 as a High-Capacity, High-Rate and Long-Life Anode Material for Lithium Ion Batteries. *Nano Energy* **2014**, *4*, 23−30.

DOI: 10.1021/acsami.5b04891
ACS Appl. Mater. Interfaces 2015, 7, 16842−16849